Title

Formation, redistribution, and stabilization of framboidal pyrite in shallowly buried deep-sea sediments

Kiichiro Kawamura
Yamaguchi University

ORCID URL
https://orcid.org/0000-0003-0501-4033

corresponding email
kiichiro@yamaguchi-u.ac.jp

“This manuscript is a non-peer-reviewed preprint submitted to EarthArXiv.”
“The manuscript is currently under peer review at Evolving Earth.”

Formation, redistribution, and stabilization of framboidal pyrite in shallowly buried deep-sea sediments

Kiichiro Kawamura [1]

[1] Graduate School of Science and Technology for Innovation, Yamaguchi University, 1677-1 Yoshida, Yamaguchi-City, Yamaguchi 753-8512, Japan

*** Correspondence:**
Corresponding Author Kiichiro Kawamura
kiichiro@yamaguchi-u.ac.jp

Keywords: Framboidal pyrite; Early diagenesis; Marine sediments; Microfabric; Geopetal fabric; Gravitational redistribution; Microfossil cavities

Abstract

Framboidal pyrite is widespread in anoxic marine sediments, but the processes that control the redistribution and preservation of pyrite aggregates after their formation remain poorly constrained. Here, I examine the microfabric and spatial organization of framboidal pyrite in shallowly buried deep-sea sediments from the Sagami Trough and the Sea of Japan using complementary freeze-dried and resin-embedded specimens. Framboidal pyrite occurs preferentially within the cavities of benthic and planktonic microfossils, where aggregates are concentrated along the lower sides of the cavities and form distinct geopetal fabrics. Loosely aggregated framboids composed of sub-spherical microcrystals occur together with densely packed framboids, indicating differences in aggregate packing and crystal development. Filamentous material less than 1 μm in thickness occurs around and between framboids within microfossil cavities, whereas isolated framboids in the surrounding sediment matrix generally lack comparable material. The preferential concentration of framboids along the lower sides of cavities is consistent with gravitational redistribution of mobile pyrite aggregates after their formation, followed by physical stabilization within confined pore spaces. The spatial association between filamentous material and pyrite further suggests that such material may have contributed to the retention of pyrite aggregates, although its composition and origin cannot be determined from the present observations. These observations indicate that the spatial organization of framboidal pyrite in marine sediments can record not only mineral formation but also subsequent physical redistribution and stabilization within sedimentary microenvironments.

1. Introduction

Pyrite (FeS_2) is one of the most common sulfide minerals in sedimentary environments and forms during early diagenesis through reactions involving reactive iron and reduced sulfur (Berner, 1984; Canfield, 1989). Framboidal pyrite is particularly widespread in modern sediments and ancient sedimentary rocks, where its size, morphology, and internal organization have been used to investigate the conditions of pyrite formation and early diagenetic environments (Wilkin et al., 1996; Ohfuji and Rickard, 2005). Framboids consist of aggregates of micrometer- to submicrometer-scale pyrite microcrystals, and their morphology reflects processes of nucleation, aggregation, crystal growth, and transformation of iron sulfide precursors (Wilkin et al., 1996; Wilkin and Barnes, 1997; Ohfuji and Rickard, 2005).

Experimental studies have demonstrated that framboidal pyrite can form through inorganic pathways involving the transformation and aggregation of iron sulfide precursors (Schoonen and Barnes, 1991; Wilkin and Barnes, 1997; Butler and Rickard, 2000). Framboidal textures can therefore develop in the absence of molecular oxygen and biological intervention, and their morphology alone does not establish a biological origin (Butler and Rickard, 2000). Consequently, observations of framboidal pyrite provide information not only on mineral formation but also on the subsequent physical and chemical processes that modify the aggregates within sediments.

Much less is known about what happens to pyrite aggregates after they form. In particular, their subsequent movement and eventual stabilization within sediment pores or microfossil cavities have received little attention. Previous studies have primarily focused on nucleation, growth, aggregation, and microarchitecture of framboidal pyrite (Wilkin et al., 1996; Wilkin and Barnes, 1997; Ohfuji and Rickard, 2005). It remains less clear how newly formed aggregates behave within confined sedimentary microenvironments and whether their subsequent spatial organization may record post-formation physical processes. This distinction is important because the final distribution of pyrite in sediment may reflect not only the conditions of mineral precipitation but also processes operating after mineral formation.

Microfossil cavities provide particularly useful three-dimensional microenvironments for examining such processes. Pyrite is known to occur within biogenic cavities and fossil tests, including foraminiferal chambers, and geopetal arrangements of pyrite have been documented in sedimentary rocks (Honjo et al., 1965; Hudson, 1982). These occurrences demonstrate that biogenic cavities can act as localized sites for authigenic pyrite accumulation and preservation. However, previous studies have generally emphasized pyrite occurrence, morphology, or fossilization rather than the possible redistribution of pre-existing pyrite aggregates within confined cavities.

Modern marine sediments provide an opportunity to examine these processes in relatively unconsolidated sedimentary systems. Although the formation and preservation of pyrite begin during

early diagenesis, the physical arrangement of pyrite aggregates may continue to evolve as the aggregates interact with pore spaces, biogenic structures, and surrounding sediment. Observations from shallowly buried sediments can therefore provide information on processes that may not be readily distinguished in lithified sedimentary rocks.

In this study, I investigate the microfabric and spatial organization of framboidal pyrite in shallowly buried deep-sea sediments from the Sagami Trough and the Sea of Japan. Using complementary freeze-drying and resin-embedding techniques, I examine (1) the morphology and aggregation state of pyrite microcrystals, (2) the spatial distribution of framboids within microfossil cavities, and (3) the occurrence and distribution of filamentous material associated with framboidal pyrite. These observations are used to evaluate the processes responsible for the formation, redistribution, and stabilization of pyrite aggregates. Particular attention is given to whether the geopetal arrangement of pyrite within microfossil cavities can be explained by post-formation gravitational redistribution.

2 Materials

Two core samples were analyzed in this study (Fig. S1). The first was collected from site 2K#942C-003 using the manned submersible *Shinkai 2000* during the NT97-10 cruise in the West Sagami Trough. This site is located at 34°59.55' N, 139°13.50' E, at a depth of 1100 m, along the West Sagami Bay Fault, approximately 500 m from an active methane seep site colonized by chemosynthetic communities (Fig. S1; Ogawa et al., 1997). It lies at the converging boundary between the Philippine Sea and North American plates. The core consists of dark gray hemipelagic clay containing about 10% framboidal pyrite by volume. The core was split in half, with one half tightly wrapped and transported to the laboratory for analysis. The sample, approximately 6 cm long and 5 cm in diameter, consists of hemipelagic clayey sediments (Fig. S2).

The second core, GC1261, with a total length of 317 cm, was collected using a gravity corer at 39°57.94' N, 138°28.96' E, at a water depth of 2509 m, during the GH99 cruise (Fig. S1; Geological Survey of Japan, 2000). This core also consists of dark gray hemipelagic clayey sediments, characterized by alternating thin laminations of dark gray, dark olive, and black, each a few millimeters thick (Fig. S2). These laminations were likely formed under fluctuating anoxic and oxic conditions during the Glacial Epoch (Tada, 1999). Notably, the black laminations contain more than 50% framboidal pyrite by volume. The core was divided into two halves onboard, and one half was used for study after being tightly wrapped and transported to the laboratory.

These two cores were selected because both contain abundant authigenic framboidal pyrite in shallowly buried fine-grained sediments, while representing contrasting deep-sea depositional settings. The Sagami Trough sample was collected near an active methane seep, whereas the Sea of

Japan sample was obtained from finely laminated sediments deposited under fluctuating redox conditions. This combination allows us to evaluate whether the observed microfabric relationships occur across different depositional settings. Both samples examined for detailed pyrite microfabric occur within the upper tens of centimeters below the seafloor.

3 Preparation of specimens

Both samples were analyzed approximately one week after collection. Until preparation, they were stored at ~4°C. Two methods were used for sample preparation: freeze-drying for scanning electron microscope (SEM) observation, and embedding for thin-section analysis (Inoue and Osatake, 1988; Kawamura and Ogawa, 2002; Kushida et al., 1988; Takizawa et al., 1995). Special care was taken to prevent oxidation and minimize disturbance of the sediment fabric caused by surface tension during drying.

Freeze-Drying Method:

First, the pore water in the sediment was replaced with ethanol, followed by t-butyl alcohol over several months. The t-butyl alcohol was then rapidly frozen using liquid nitrogen, and the sample was sublimated in a vacuum desiccator. This method preserved the original microfabric, ensuring minimal disturbance, making the sample suitable for SEM observation. The sample was coated with Au-Pd for SEM imaging, conducted at 15 to 20 kV and ~80 μA.

Embedding Method for Thin Sections:

In this method, the pore water was replaced with ethanol, followed by propylene oxide over several months. The propylene oxide was then replaced with Quetol 651 resin (Nisshin EM Co. Ltd.), and the sediment was cured at 60°C for 24 hours to produce thin sections. Framboidal pyrites were analyzed using energy-dispersive spectrometry (EDS) at 15 kV and ~1.2 μA, while elemental mapping was performed using wave-dispersive spectrometry (WDS) at 15 kV and ~5.0 μA.

4 Results

Some of the specimens examined in this study were previously documented by Kawamura et al. (1999), but their spatial organization within microfossil cavities is re-examined here in the context of post-formation redistribution and stabilization.

Small opaque particles were observed in two sediment samples: at 3 cm below the seafloor (cm-bsf) in core 2K#942C-003 and at 30 cm-bsf in core GC1261 (Figs. 1A–I, S3). These particles were identified as pyrite, exhibiting a bright yellowish color in reflected light microscopy (Figs. 1B,

S6), high reflectivity in backscattered electron images (indicative of heavy elements; Figs. 1J–K, 2G–H, S4, S7–S9), and Fe and S as the major elements in energy dispersive spectroscopy (EDS) analyses (Figs. 1J–K, S3, S8, S9; Table S1). Pyrite in both 2K#942C-003 and GC1261 occurred as both framboidal aggregates and isolated submicrometer crystallites in microspaces and within microfossils (Figs. 2B,K, S6–S9). In GC1261, they were aligned along parallel laminations (Figs. 1H–I, S3).

Based on resin thin section observations, the majority of the pyrite grains were framboids with diameters ranging from 5 to 10 μm (Figs. 1, S4–S9). A smaller portion consisted of crystallites less than 1 μm in size (Figs. 2, S4–S9).

In GC1261, spherical cores smaller than 1 μm were observed scattered around the framboidal pyrite. Some of these cores formed loosely packed framboids, approximately 5 μm in diameter (Figs. 2D, 2H, S4–S5). The loose framboids consisted of subangular or subspherical cores, contrasting with the typical angular (euhedral) crystallites in fully formed framboidal pyrite. The subspherical cores were flattened only at contact surfaces between triangular, rectangular, or hexagonal grains, while retaining spherical shapes at free surfaces (Figs. 2D, S5).

Framboidal pyrite was densely packed within the cavities of benthic and planktonic microfossils and preferentially accumulated along the lower parts of the cavities, parallel to the bedding plane (Figs. 1A–J, 2A–C, S6). This arrangement constitutes a geopetal fabric, with framboidal pyrite preferentially concentrated along the lower sides of the microfossil cavities. This arrangement was observed repeatedly in the examined microfossil cavities (Figs. 1, 2).

The framboidal pyrite within microfossils was covered by filamentous material (Figs. 2A–C, 2E–F), while isolated framboidal pyrite in the sediment matrix was not (Figs. 2D, S5). This filamentous material, less than 1 μm thick, connected adjacent framboidal pyrite grains, forming a network (Figs. 2A–C). In some cases, the filamentous material completely enveloped the framboidal pyrite grains (Figs. 2E–F).

5. Discussion

5.1. Formation and aggregation of framboidal pyrite

The coexistence of loosely aggregated and densely packed framboids provides constraints on the development of pyrite aggregates in the studied sediments. Loosely aggregated framboids consist of sub-spherical or subangular microcrystals, whereas more densely packed aggregates contain crystals with more developed and locally euhedral morphologies. Experimental studies have demonstrated that framboidal pyrite can develop through the nucleation and transformation of iron sulfide precursors followed by aggregation and subsequent conversion to pyrite (Schoonen and Barnes, 1991; Wilkin and Barnes, 1997; Butler and Rickard, 2000). The difference between the two types of

framboids suggests different degrees of aggregation and crystal development. The textures alone, however, do not allow us to determine whether one formed before the other.

The formation of framboidal pyrite has been attributed to both inorganic and biologically mediated processes (Sweeney and Kaplan, 1973; Wilkin and Barnes, 1997; Ohfuji and Rickard, 2005). Experimental studies have shown that framboidal textures can form in the absence of biological intervention, demonstrating that morphology alone cannot be used to infer a biological origin (Butler and Rickard, 2000). The present observations likewise do not require a biological mechanism for the formation of the framboids. Instead, they indicate that pyrite aggregates can occur in different states of packing and crystal development within shallowly buried marine sediments. The subsequent spatial organization of these aggregates therefore provides an additional record of processes operating after their initial formation.

5.2. Gravitational redistribution of pyrite aggregates within microfossil cavities

The preferential concentration of framboidal pyrite along the lower sides of microfossil cavities suggests post-formation redistribution of pyrite aggregates. Geopetal arrangements of pyrite have previously been documented in sedimentary rocks, demonstrating that the spatial orientation of pyrite within cavities can preserve information on the relative position of the host cavity during or after mineral formation (Honjo et al., 1965). However, the observations in the present study provide an opportunity to consider a different process: the redistribution of pre-existing pyrite aggregates within confined cavities.

Framboids were not distributed uniformly within the cavities. Instead, they were concentrated on the lower side, whereas the upper part of the cavities was commonly free of framboids. This pattern was observed in several cavities. If the framboids had formed entirely in place, it would be difficult to account for this repeated asymmetry. A more straightforward interpretation is that at least some aggregates were mobile after formation and moved toward the lower part of the cavity. The observed fabric is therefore not necessarily a primary precipitation fabric. Rather, it may record movement of already formed aggregates within the cavity.

The occurrence of loosely aggregated framboids elsewhere in the sediment is consistent with the presence of relatively mobile pyrite aggregates. Once such aggregates entered a confined microfossil cavity, their movement would have been restricted by the cavity geometry, while gravity would favor accumulation along the lower cavity wall. The resulting arrangement would produce the observed geopetal fabric. I interpret the geopetal fabrics as being consistent with a sequence involving initial pyrite aggregate formation, subsequent gravitational redistribution, and eventual stabilization within confined pore spaces.

This interpretation does not exclude alternative processes, including local mineral

231 precipitation or pore-fluid movement. Nevertheless, the repeated concentration of aggregates along
232 the lower sides of multiple cavities is consistent with gravitational redistribution of mobile aggregates
233 and is difficult to explain by random in situ precipitation alone. The observations therefore suggest
234 that post-formation physical redistribution should be considered when interpreting the spatial
235 organization of framboidal pyrite in sedimentary microenvironments.
236
237 5.3. Stabilization of framboidal pyrite by filamentous material
238
239 A distinctive feature of the studied samples is the occurrence of filamentous material around
240 and between framboidal pyrite aggregates within microfossil cavities. The material is less than 1 μm
241 in thickness and locally forms a network that surrounds individual framboids. In contrast, isolated
242 framboids in the surrounding sediment matrix generally lack comparable filamentous structures. The
243 spatial association is consistent with a possible physical coupling between pyrite aggregations and
244 surrounding filamentous material during very early sedimentary processes.
245 Pyrite–organic matter associations have been documented in natural geological
246 environments, indicating that organic materials can occur in close spatial association with pyrite during
247 mineral formation and preservation (Raiswell and Canfield, 1991; Lindgren et al., 2011). Such
248 associations, however, do not by themselves establish a biological origin for either the pyrite or the
249 associated material.
250 The composition and origin of the filamentous material cannot be determined from the
251 present observations. Its morphology alone is insufficient to identify it as microbial. It may represent
252 organic-rich material, microbial-derived material, or another filamentous phase that formed or
253 persisted within the sediment. Regardless of its origin, its repeated occurrence around framboids
254 within the cavities, and its absence around isolated framboids in the surrounding matrix, suggests that
255 it may have contributed to the retention of the aggregates.
256
257 5.4. Implications for Fe–S mineral–organic interfaces and early Earth chemistry
258
259 The observations described above also have implications for the preservation of spatial
260 associations between Fe–S minerals and surrounding materials in marine sediments. The concentration
261 of framboidal pyrite within confined microfossil cavities, together with the occurrence of filamentous
262 material around and between the aggregates, indicates that mineral aggregates can become physically
263 associated with materials present within sedimentary microenvironments. Although the composition
264 and origin of the filamentous material cannot be determined from the present observations, its
265 distribution is consistent with a possible role in restricting aggregate mobility and promoting their
266 retention within the cavities.

More broadly, the results indicate that the preservation of pyrite microfabric may reflect a combination of mineral formation and subsequent physical processes. The observed sequence of aggregation, gravitational redistribution, and stabilization provides a mechanism by which Fe–S mineral aggregates can become spatially concentrated and preserved within marine sediments. This physical component should be considered alongside chemical and biological processes when interpreting the microfabric and spatial distribution of authigenic pyrite in the sedimentary record.

6. Conclusions

(1) Framboidal pyrite in shallowly buried deep-sea sediments occurs as both loosely aggregated and densely packed aggregates, consistent with differences in the degree of pyrite microcrystal aggregation and development.

(2) Framboidal pyrite is preferentially concentrated along the lower sides of microfossil cavities, producing distinct geopetal fabrics. This spatial organization is consistent with gravitational redistribution of mobile pyrite aggregates after their initial formation.

(3) Filamentous material less than 1 μm in thickness occurs preferentially around and between framboidal pyrite aggregates within microfossil cavities. Although its composition and origin remain unresolved, its spatial association with pyrite is consistent with a possible role in the physical retention and stabilization of the aggregates.

(4) The observations support a model involving pyrite aggregate formation, subsequent redistribution within confined pore spaces, and physical stabilization. The results demonstrate that the spatial organization of framboidal pyrite in shallowly buried marine sediments can reflect post-formation physical processes in addition to the conditions of mineral formation.

(5) These observations provide microfabric-based constraints on the early diagenetic modification and preservation of authigenic pyrite. In particular, gravitational redistribution and subsequent stabilization within sedimentary microenvironments should be considered when interpreting geopetal and other spatially organized pyrite fabrics in the sedimentary record.

6 Author Contributions

Kiichiro Kawamura: Conceptualization, investigation, methodology, data curation, visualization, and writing—original draft and review and editing.

7 Funding

Part of the study was supported by a Grant-in-Aid from Japan Society for the Promotion of Science (JSPS) for Scientific Research (B-14740295).

8 Acknowledgments

I would like to express my sincere gratitude to Professor Yujiro Ogawa and Dr. Tadashi Sato for their constructive feedback on an early draft of this work. Special thanks go to Dr. Hidetsugu Taniguchi and Ms. T. Kawata for their assistance with SEM observations and EDS analyses. I also thank Dr. Ken Ikehara for providing the GC1261 sample and Professor Takeshi Naganuma for his valuable suggestions on biotic processes in the deep sea.

Declaration of Generative AI and AI-assisted technologies in the writing process

During the preparation of this manuscript, the author used ChatGPT (OpenAI) to assist with language editing, English expression, and manuscript organization. The author reviewed and edited all AI-assisted output and takes full responsibility for the content, interpretations, and conclusions of the manuscript.

Data availability

The research data supporting the findings of this study, including the analytical data and digital image data underlying the photomicrographs, SEM, BSE, and EDS observations, are openly available in Mendeley Data at Kawamura, Kiichiro (2026), “ResearchDataKawamura2026FramboidalPyrites”, Mendeley Data, V1, doi: 10.17632/xtfsrxyy5t.1.

9 References

Berner, R.A., 1984. Sedimentary pyrite formation: An update. Geochim. Cosmochim. Acta 48, 605–615. https://doi.org/10.1016/0016-7037(84)90089-9.

Butler, I.B., Rickard, D., 2000. Framboidal pyrite formation via the oxidation of iron (II) monosulfide by hydrogen sulphide. Geochim. Cosmochim. Acta 64, 2665–2672. https://doi.org/10.1016/S0016-7037(00)00387-2.

Canfield, D.E., 1989. Reactive iron in marine sediments. Geochim. Cosmochim. Acta 53, 619–632. https://doi.org/10.1016/0016-7037(89)90005-7.

Honjo, S., Fischer, A.G., Garrison, R., 1965. Geopetal pyrite in fine-grained limestones. J. Sediment. Petrol. 35, 480–488. https://doi.org/10.1306/74D712B2-2B21-11D7-8648000102C1865D.

Hudson, J.D., 1982. Pyrite in ammonite-bearing shales from the Jurassic of England and Germany. Sedimentology 29, 639–667. https://doi.org/10.1111/j.1365-3091.1982.tb00072.x.

Inoue, T., Osatake, H., 1988. A new drying method of biological specimens for scanning electron microscopy: The t-butyl alcohol freeze-drying method. Arch. Histol. Cytol. 51, 53–59. https://doi.org/10.1679/aohc.51.53.

Geological Survey of Japan, 2000. Comprehensive study on environmental changes in the western Hokkaido coastal area and study on evaluation of marine active faults: preliminary reports on

researches in the 1999 fiscal year. GSJ Interim Report MG/00/1, 211 pp.

Kawamura, K., Ogawa, Y., 2002. Progressive microfabric changes in unconsolidated pelagic and hemipelagic sediments down to 180 mbsf, Northwest Pacific, ODP Leg 185, Site 1149. In: Ludden, J.N., Plank, T., Escutia, D. (Eds.), Proceedings of the Ocean Drilling Program, Scientific Results 185. https://doi.org/10.2973/odp.proc.sr.185.003.2002.

Kawamura, K., Ogawa, Y., Kawata, T., 1999. Observation of freeze-dried and embedded deep-sea muds from Sagami Bay by SEM-EDS. JAMSTEC J. Deep Sea Res. 14, 329–344.

Kushida, T., Iijima, H., Kushida, H., Tsuruta, C., 1988. An improved embedding method employing epoxy resin Quetol 651 for stereoscopic observation of thick sections under a 300 KV transmission electron microscope. J. Electron Microsc. 37, 212–214. https://doi.org/10.1093/oxfordjournals.jmicro.a050688.

Lindgren, P., Parnell, J., Holm, N.G., Broman, C., 2011. A demonstration of an affinity between pyrite and organic matter in a hydrothermal setting. Geochem. Trans. 12, 3. https://doi.org/10.1186/1467-4866-12-3.

Ogawa, Y., Fujiwara, Y., Hunt, J.C., Iwase, R., Kaneko, H., Kawamura, K., Kitazato, H., Kobayashi, H., Koizumi, K., Kubota, S., Nishida, S., Ohtsuka, T., Shimanaga, M., Takaki, Y., Tsuchida, S., Tsuchiya, M., Uematsu, K., Yamamoto, T., Hashimoto, J., Segawa, J., 1997. Preliminary report of "Shinkai 2000" May 1997 Sagami Bay mission—dives 939 to 945. JAMSTEC J. Deep Sea Res. 13, 354–370.

Ohfuji, H., Rickard, D., 2005. Experimental syntheses of framboids—a review. Earth-Sci. Rev. 71, 147–170. https://doi.org/10.1016/j.earscirev.2005.02.001.

Raiswell, R., Canfield, D.E., 1991. Pyrite formation and fossil preservation. In: Allison, P.A., Briggs, D.E.G. (Eds.), Taphonomy: Releasing the Data Locked in the Fossil Record. Plenum Press, New York, pp. 337–387. https://doi.org/10.1007/978-1-4899-5034-5_7.

Schoonen, M.A.A., Barnes, H.L., 1991. Reactions forming pyrite and marcasite from solution: I. Nucleation of FeS_2 below 100 °C. Geochim. Cosmochim. Acta 55, 1495–1504. https://doi.org/10.1016/0016-7037(91)90122-L.

Sweeney, R.E., Kaplan, I.R., 1973. Pyrite framboid formation: laboratory synthesis and marine sediment. Econ. Geol. 68, 618–634. https://doi.org/10.2113/gsecongeo.68.5.618.

Takizawa, S., Kawata, T., Ohno, Y., 1995. A method of fixation and freeze-drying of soft sediments containing water. J. Geol. Soc. Jpn. 101, 941–944. https://doi.org/10.5575/GEOSOC.101.941.

Tada, R., 1999. Late Quaternary paleoceanography of the Japan Sea: an update. Quat. Res. 38, 216–222. https://doi.org/10.4116/jaqua.38.216.

Wilkin, R.T., Barnes, H.L., Brantley, S.L., 1996. The size distribution of framboidal pyrite in modern sediments: an indicator of redox conditions. Geochim. Cosmochim. Acta 60, 3897–3912. https://doi.org/10.1016/0016-7037(96)00209-8.

Wilkin, R.T., Barnes, H.L., 1997. Formation process of framboidal pyrite. Geochim. Cosmochim. Acta 61, 323–339. https://doi.org/10.1016/S0016-7037(96)00320-1

FIGURE CAPTIONS

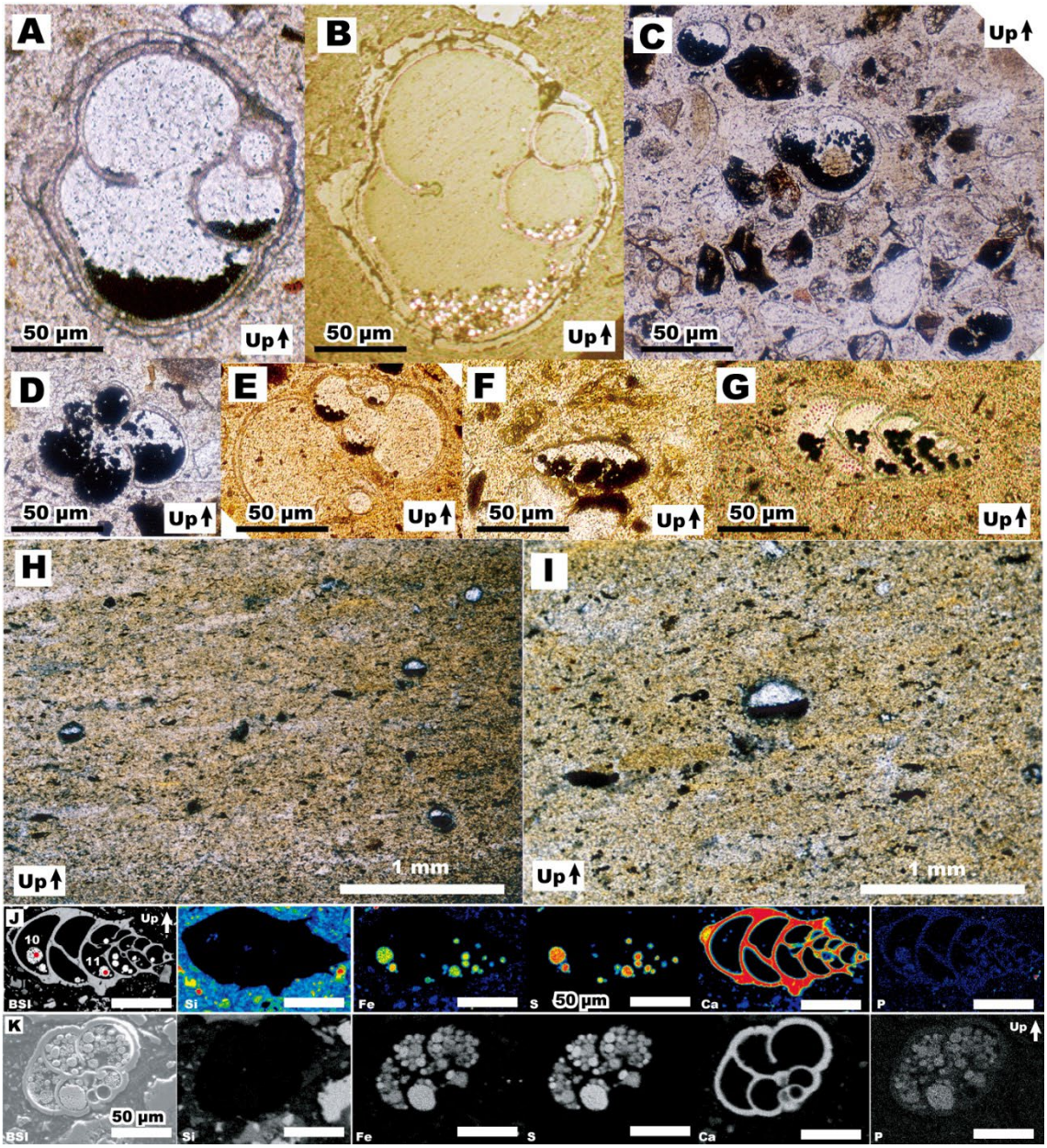

Figure 1. Pyrite microtextures of embedded samples, vertical view. Arrows show the upward direction. A–F: Geopetal fabric of framboidal pyrite in benthic foraminifers in 3 cm-bsf, 2K#942C-003, the Sagami Trough, thin section, open nicol (previously published by Kawamura et al., 1999; reinterpreted in this study). B: Reflected light image of A (Kawamura et al., 1999). H and I: Framboidal pyrites along parallel laminations at 53.76 cm-bsf, GC1261, the Sea of Japan. J and K: Pyrite microtextures in back-scattering image (BSI) and element mapping image (Si, Fe, S, Ca and P) on polished section of embedded samples at 3 cm-bsf, 2K#942C-003, the Sagami Trough. J and K were measured at Figs. 1G and S6A using WDS and EDS, respectively. The analyzed numbers in J correspond to the number shown in Table S1.

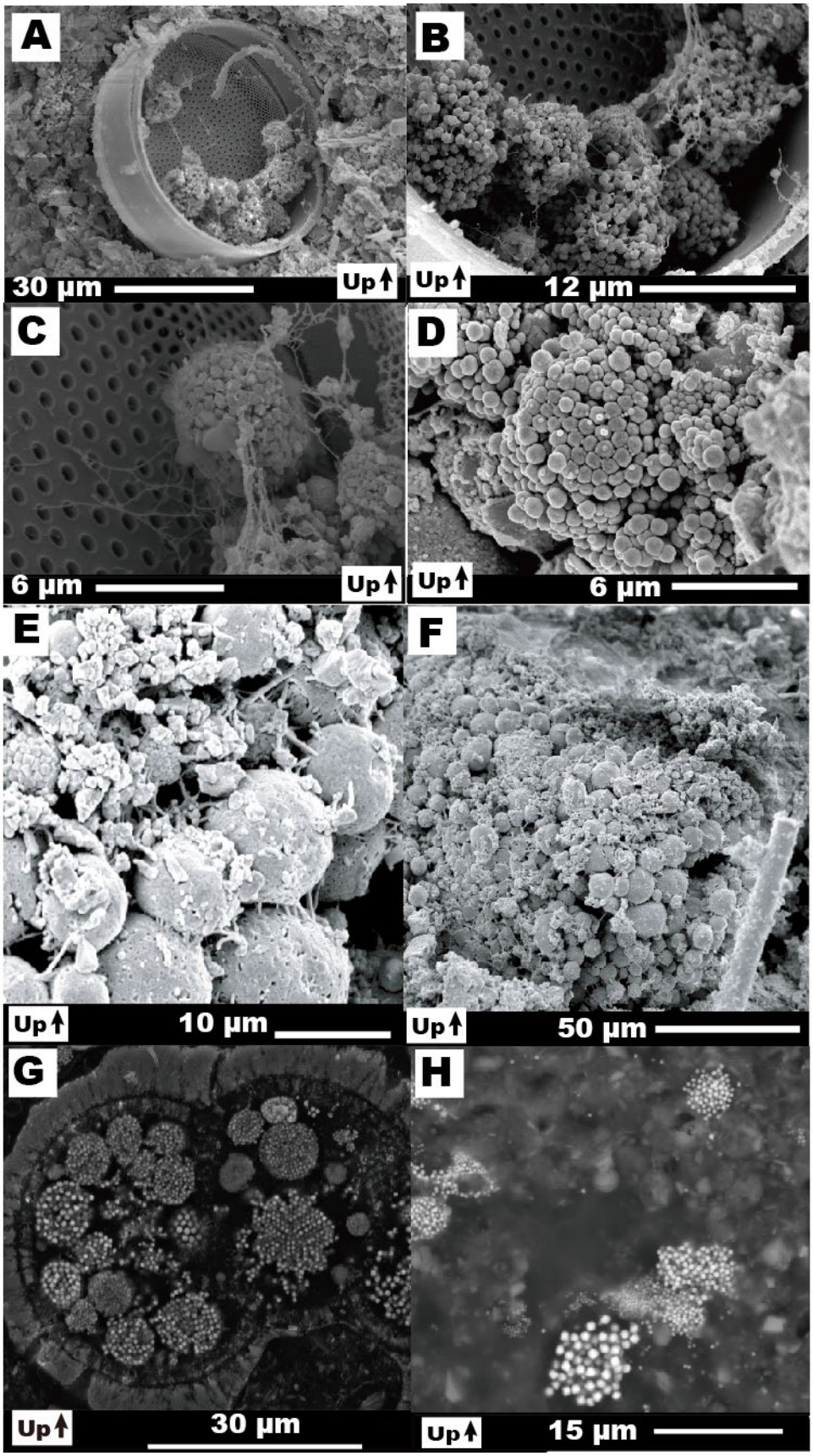
A
30 µm
Up
B
Up
12 µm
C
6 µm
Up
D
Up
6 µm
E
Up
10 µm
F
Up
50 µm
G
Up
30 µm
H
Up
15 µm

390

391 Figure 2. Pyrite microtextures, vertical view. Arrows show the upward direction. A, B and C: Geopetal
392 fabric in diatoms filled by framboidal pyrite at 30 cm-bsf, GC1261, the Sea of Japan, secondary
393 electron image, freeze-dried samples. D: Loose framboids with spherical microcrystals at 30 cm-bsf,
394 GC1261, the Sea of Japan, secondary electron image, freeze-dried samples. E and F: Framboidal
395 pyrites in a diatom at 3 cm-bsf, 2K#942C-003, the Sagami Trough, secondary electron image, freeze-
396 dried samples. G: Pyrite microtextures in back-scattering image (BSI) on polished section of
397 embedded samples at 3 cm-bsf, 2K#942C-003, the Sagami Trough, vertical view. H: Pyrite
398 microtextures in back-scattering image (BSI) on polished section of embedded samples at 30 cm-bsf,
399 GC1261, the Sea of Japan, vertical view. The pyrite microcrystals in H are loosely aggregated.
400 Filamentous material occurs around framboidal pyrite within microfossils in A–C and E–F.
401

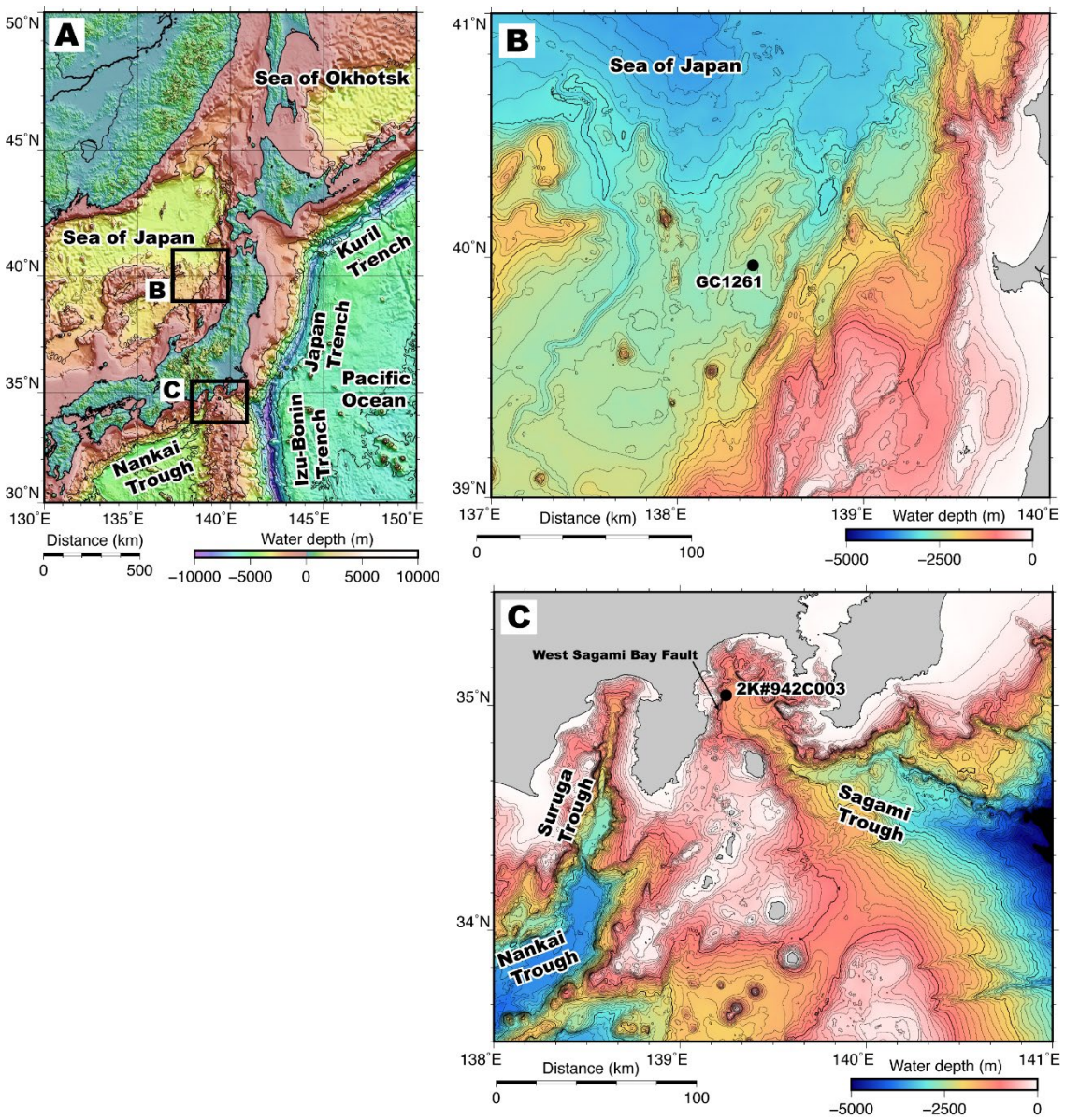

Figure S1 Coring sites of the studied specimens. A: Locality of the coring sites of GC1261 (B) and 2K#942C-003 (C). B: Coring site of GC1261, located on a spur. C: Coring site of 2K#942C-003, located on the West Sagami Bay Fault, which forms the western boundary of the Sagami Trough.

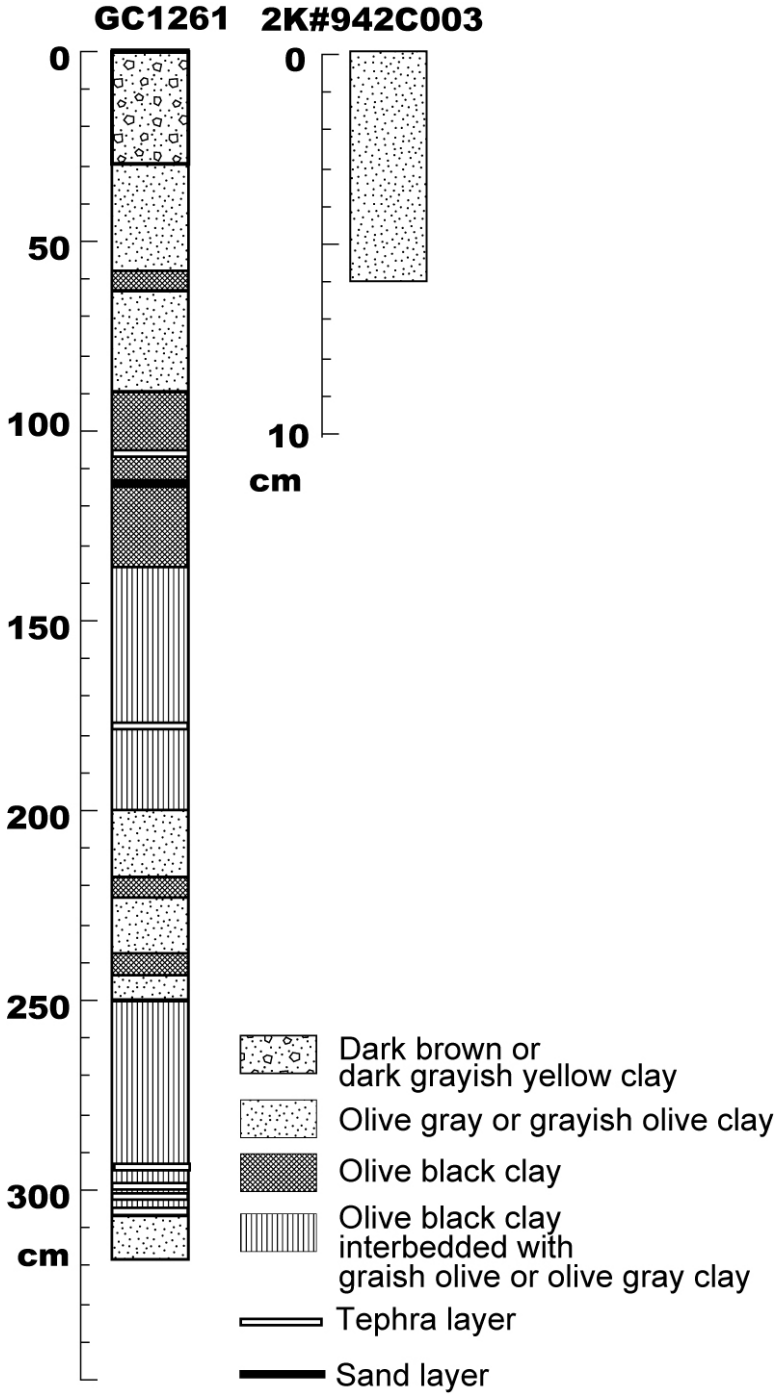

409
410
411

412 Figure S2 Sedimentological columns of the studied specimens GC1261 and 2K#942C-
413 003. The column of GC1261 is modified from Geological Survey of Japan (2000).

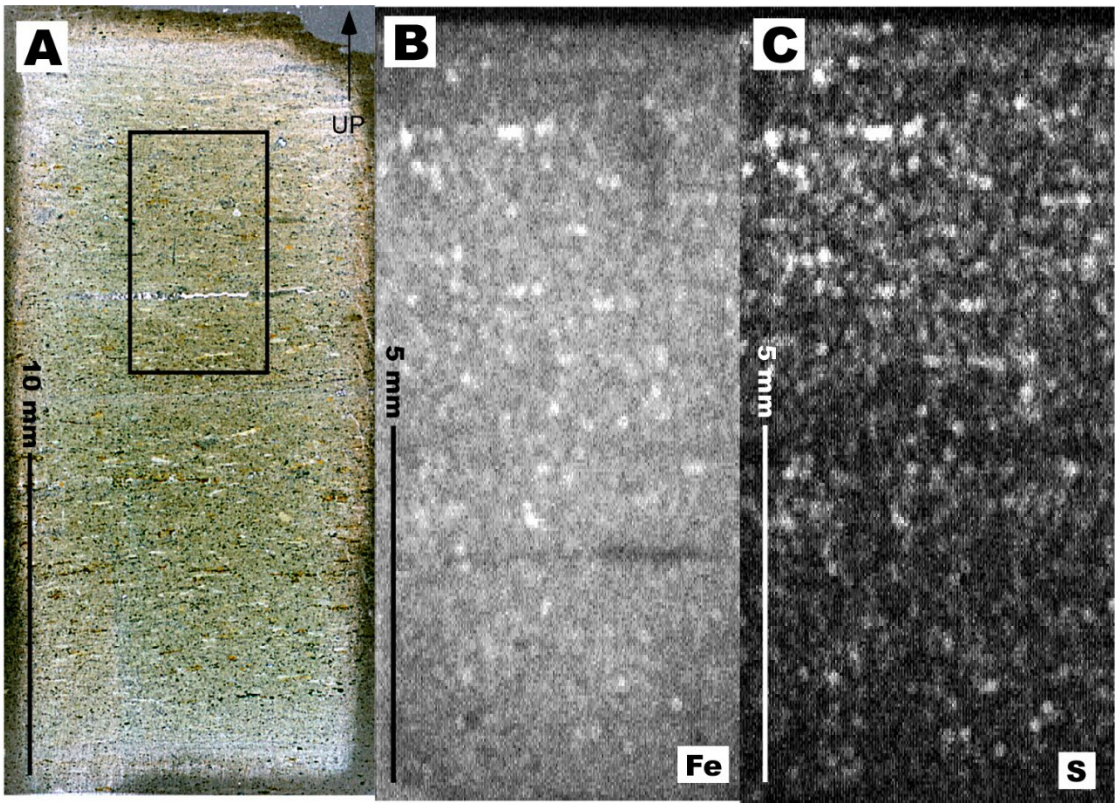

Figure S3 Detailed sedimentary structures (A) and element-mapping images (Fe in B and S in C) at 30 cm in GC1261, vertical view. Arrows show the upward direction. Pyrite, identified by the co-occurrence of Fe and S, is concentrated along parallel laminations. The element mapping was conducted by energy dispersive X-ray spectroscopy at a setting of 15 kV and approximately 1 μA.

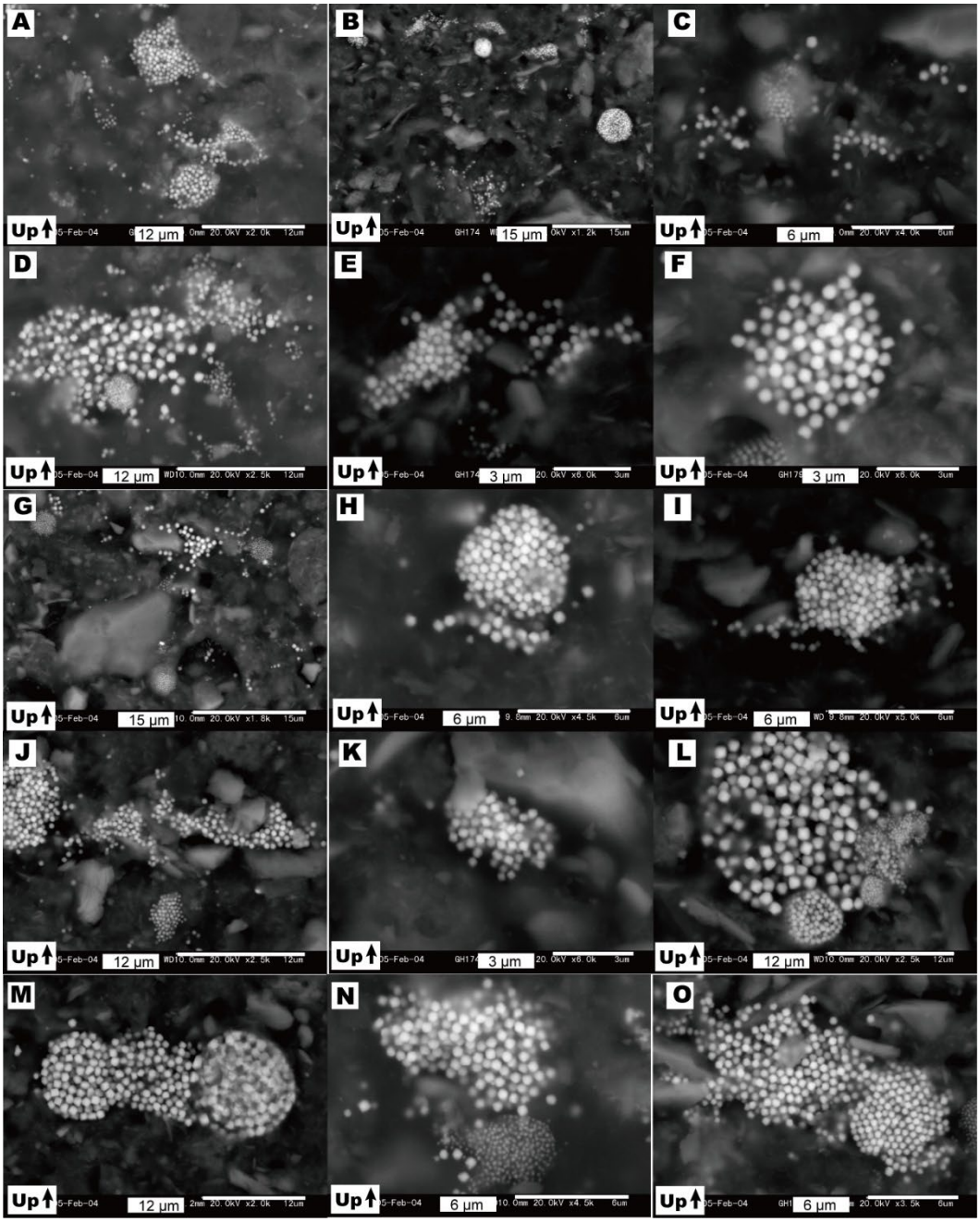

Figure S4 Pyrite microtextures in back-scattering image (BSI) on polished section of embedded samples at 30 cm-bsf, GC1261, the Sea of Japan, vertical view. Arrows show the upward direction. The pyrite microcrystals are loosely aggregated. Some pyrite microcrystals form thread-like arrangements (C), and most of them are arranged horizontally along the laminations (B, I, and J). Images were acquired at 20 kV to enhance the surface relief of pyrite microcrystals within the resin.

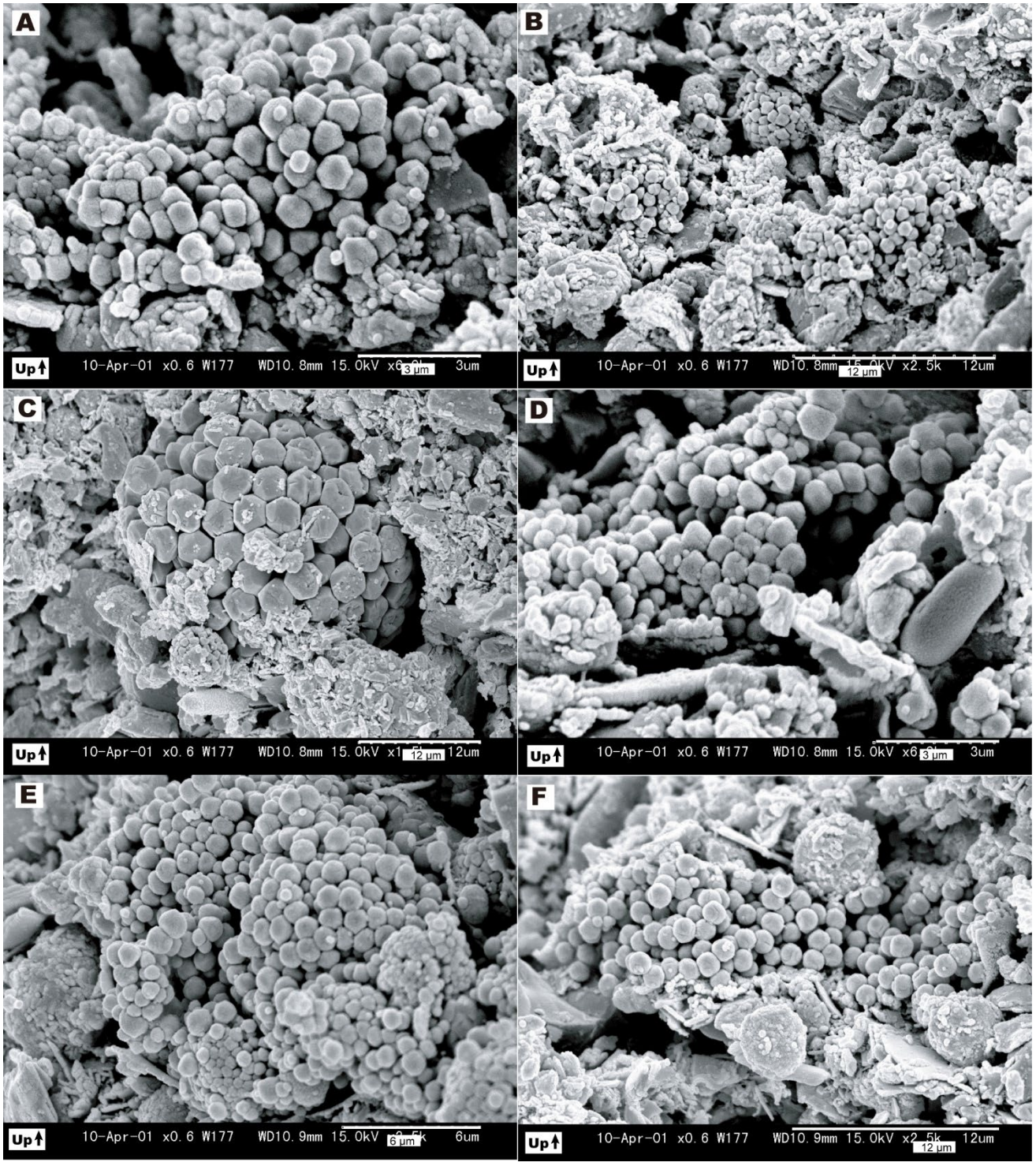

Figure S5 Pyrite microtextures in secondary electron image, freeze-dried samples at 30 cm-bsf, GC1261, the Sea of Japan, vertical view. Arrows show the upward direction. The pyrite microcrystals are loosely aggregated and show spherical to angular morphologies.

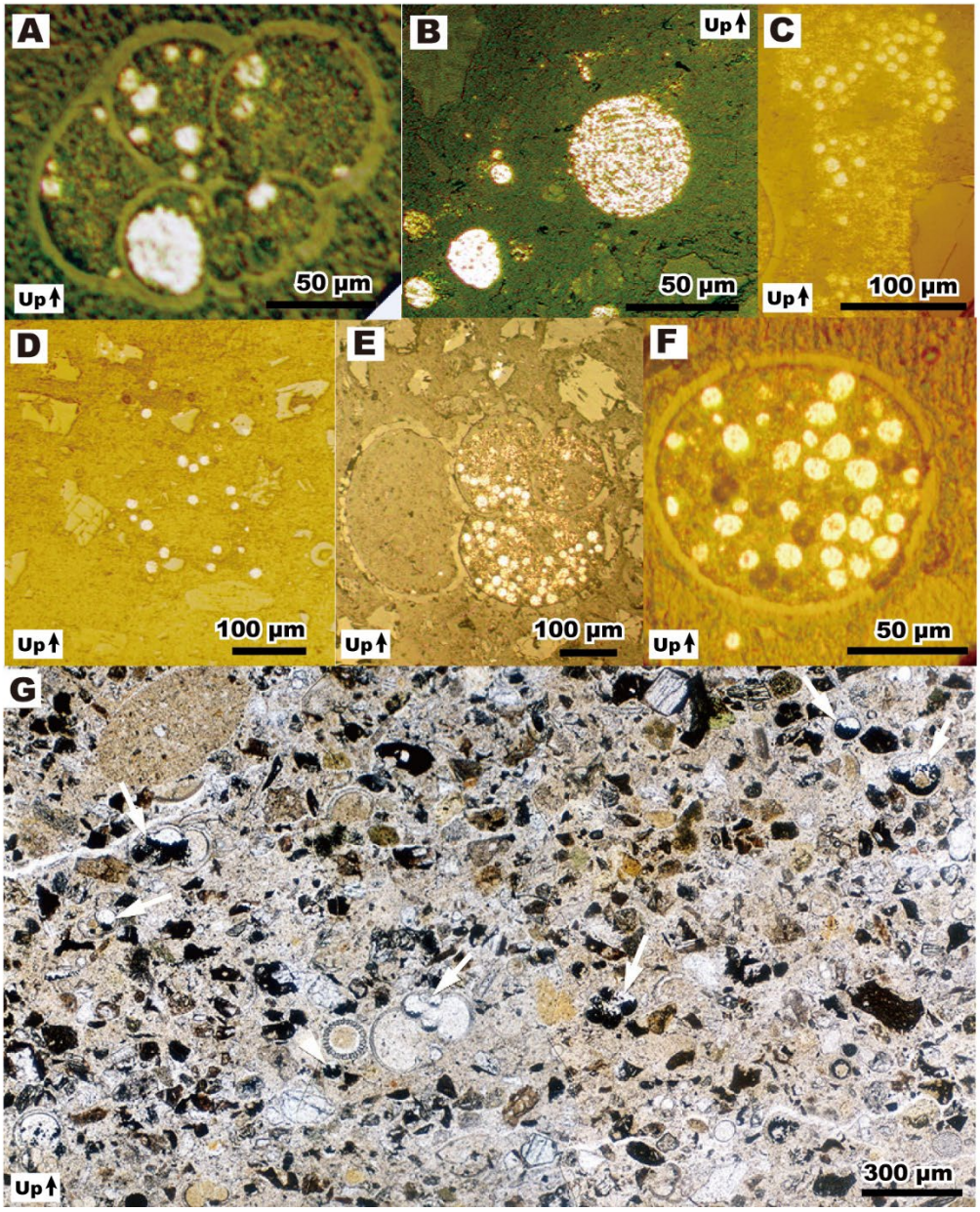

Figure S6 Pyrite microtextures in optical and reflected images. Arrows show the upward direction. A–F: Reflected light images in 3 cm-bsf, 2K#942C-003, the Sagami Trough, thin section, open nicol (Reproduced from Kawamura et al., 1999). G: Geopetal fabric of framboidal pyrite in planktic foraminifers in 3 cm-bsf, 2K#942C-003, the Sagami Trough, thin section, open nicol (Reproduced from Kawamura et al., 1999).

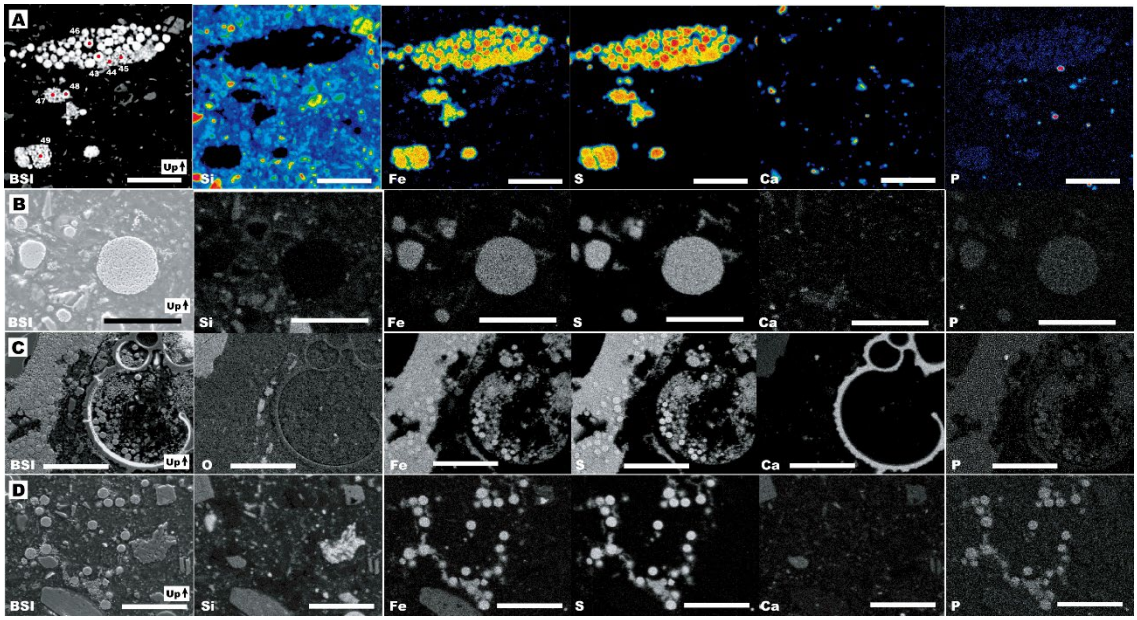

Figure S7 Pyrite microtextures in back-scattering image (BSI) and element mapping images on polished section of embedded samples at 30 cm-bsf, GC1261 (A) and 3 cm-bsf, 2K#942C-003, the Sagami Trough (B-D), vertical view. Arrows show the upward direction. Elemental mapping and compositional analyses in A were conducted using WDS, whereas those in B–D were conducted using EDS. The analyzed numbers in A correspond to the number shown in Table S1. Scale bars are 50 μm.

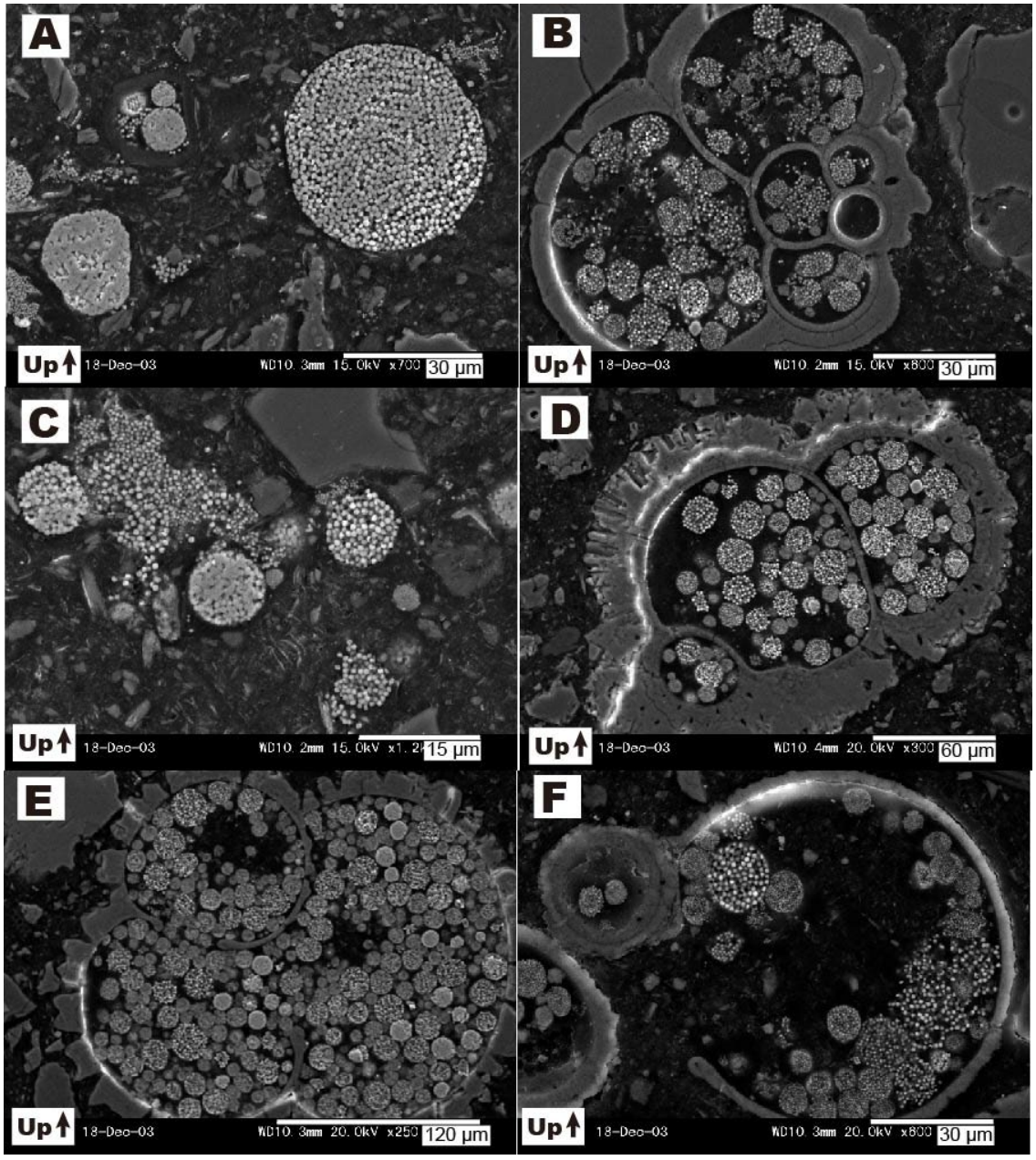

456

457

458

459 Figure S8 Pyrite microtextures in back-scattering images (BSI) on polished section of
460 embedded samples at 30 cm-bsf, GC1261, the Sea of Japan (A) and at 3 cm-bsf, 2K#942C-
461 003, the Sagami Trough (B–D), vertical view. Arrows show the upward direction.

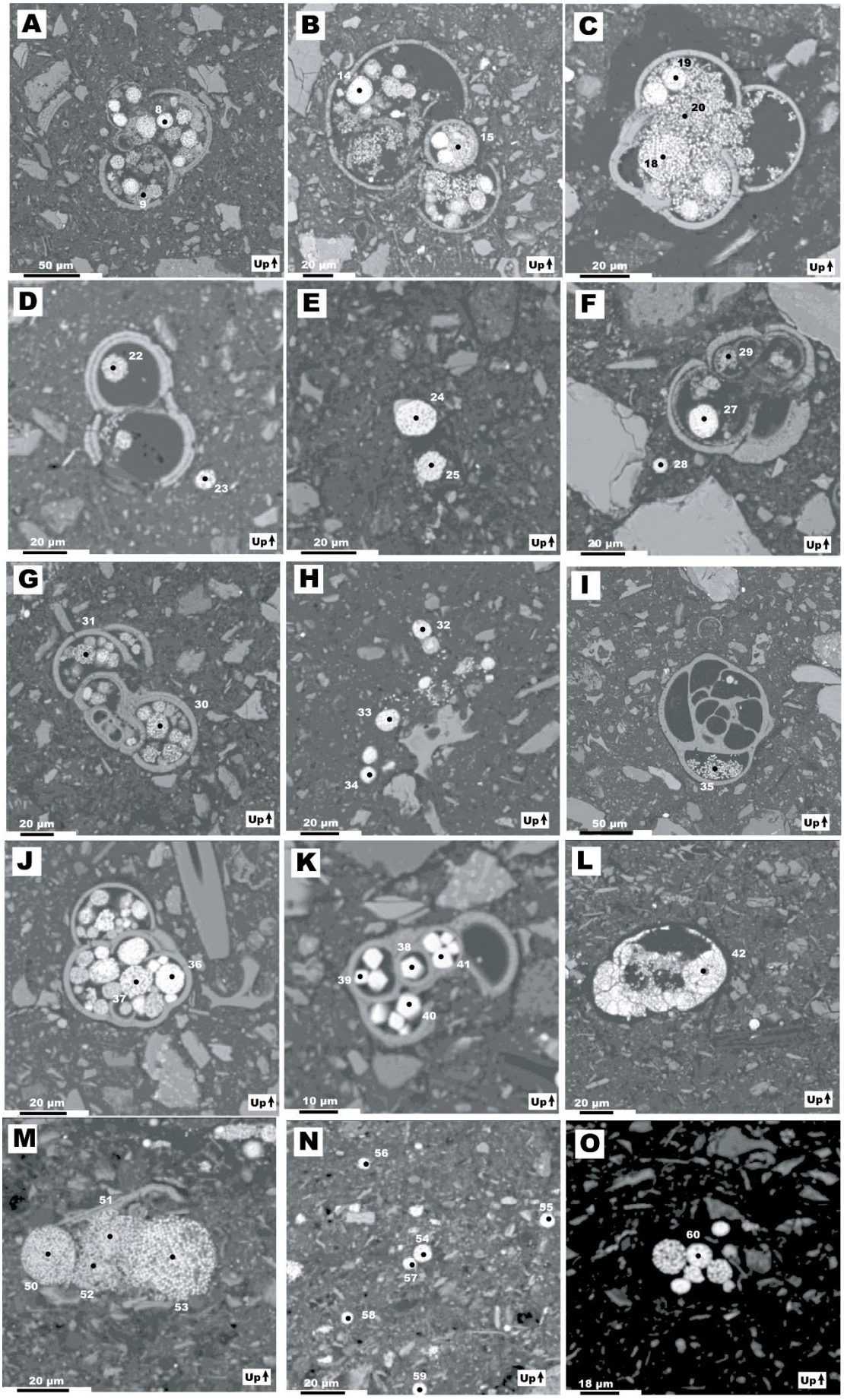
A
8
9
50 µm
Up
B
14
15
20 µm
Up
C
19
20
18
20 µm
Up
D
22
23
20 µm
Up
E
24
25
20 µm
Up
F
29
27
28
20 µm
Up
G
31
30
20 µm
Up
H
32
33
34
20 µm
Up
I
35
50 µm
Up
J
36
37
20 µm
Up
K
38
41
39
40
10 µm
Up
L
42
20 µm
Up
M
51
50
52
53
20 µm
Up
N
56
55
54
57
58
59
20 µm
Up
O
60
18 µm
Up

Figure S9 Pyrite microtextures in back-scattering image (BSI) on polished section of embedded samples with measurement points at 3 cm-bsf, 2K#942C-003, the Sagami Trough (A–K) and at 30 cm-bsf, GC1261, the Sea of Japan (L–O), vertical view. Arrows show the upward direction. The elemental analyses were conducted using WDS. The analyzed numbers correspond to the number shown in Table S1.

Table S1. Results of WDS analyses of pyrite microcrystals and framboids. Numbers indicate the measurement points shown in Fig. 1J, Fig. S7A, and Fig. S9. Samples from 3 cm-bsf in 2K#942C-003 and 30 cm-bsf in GC1261 correspond to measurement points 8–41 and 42–60, respectively.

No.	P	Fe	S	Fe/S
8	0.00	32.94	67.06	0.49
9	0.00	37.68	62.32	0.60
10	0.06	32.77	67.17	0.49
11	0.02	34.25	65.73	0.52
14	0.03	34.04	65.93	0.52
15	0.06	33.15	66.80	0.50
18	0.02	33.12	66.87	0.50
19	0.05	33.93	66.02	0.51
20	0.03	33.68	66.29	0.51
22	0.01	36.35	63.65	0.57
23	0.01	33.13	66.86	0.50
24	0.00	33.36	66.64	0.50
25	0.02	32.35	67.63	0.48
27	0.00	33.14	66.86	0.50
28	0.00	33.14	66.85	0.50
29	0.00	37.37	62.63	0.60
30	0.00	35.94	64.06	0.56
31	0.00	33.23	66.77	0.50
32	0.00	32.85	67.15	0.49
33	0.01	33.42	66.56	0.50
34	0.00	32.72	67.28	0.49
35	0.01	33.62	66.37	0.51
36	0.01	33.08	66.91	0.49
37	0.02	33.52	66.46	0.50
38	0.00	32.63	67.37	0.48
39	0.03	32.79	67.17	0.49
40	0.00	32.86	67.14	0.49
41	0.00	32.44	67.56	0.48
42	0.01	34.56	65.43	0.53
43	0.03	35.23	64.74	0.54
44	0.01	33.03	66.96	0.49
45	0.02	34.65	65.33	0.53
46	0.01	33.81	66.19	0.51
47	0.01	32.33	67.66	0.48
48	0.00	33.11	66.89	0.49
49	0.03	34.94	65.03	0.54
50	0.00	36.63	63.37	0.58
51	0.02	35.92	64.06	0.56
52	0.00	35.34	64.66	0.55
53	0.01	31.86	68.12	0.47
54	0.00	34.06	65.94	0.52
55	0.08	36.86	63.06	0.58
56	0.02	34.05	65.93	0.52
57	0.00	35.13	64.87	0.54
58	0.02	32.26	67.72	0.48
59	0.00	33.04	66.96	0.49
60	0.00	32.66	67.34	0.49